Article

Post-Synthetic Doping and Ligand Engineering of $Cs_2AgInCl_6$ Double Perovskite Nanocrystals

Published as part of The Journal of Physical Chemistry C virtual special issue "The Physical Chemistry of Perovskites".

Lacie Dube, Peter Saghy, and Ou Chen*

ABSTRACT: Lead-free double perovskite (DP) nanocrystals (NCs) have emerged as a promising class of perovskite nanomaterials with potential applications in various optical and optoelectronic domains. Meanwhile, doping impurity ions into perovskite structures represents a unique and effective means to tailor and optimize the properties of perovskite materials. Herein, we introduce a postsynthetic doping approach to the fabrication of Mn^{2+}-doped $Cs_2AgInCl_6$ DP NCs with enhanced optical characteristics. We demonstrate that, in the postsynthetic reaction, the initial surface-doped Mn^{2+} ions undergo a gradual inward migration process within the NCs, resulting in homogeneous Mn^{2+} doping with a maximum photoluminescence (PL) quantum yield (QY) of 5.2%. This PL QY value can be further improved to 8.2% through codoping with Na^+ ions and careful engineering of the NC surface state. In-depth studies involving conventional one-dimensional proton and two-dimensional NMR spectroscopic techniques unveil the pivotal role played by the surface ligands and their states. Based on our findings, we propose a comprehensive postsynthetic doping mechanism. Our study not only presents an accessible doping technique for lead-free perovskite NCs but also offers valuable insights into the dopant dynamics and ligand engineering for perovskite-type nanomaterials in a broader context.

Post-Synthetic Codoping of Double Perovskite NCs
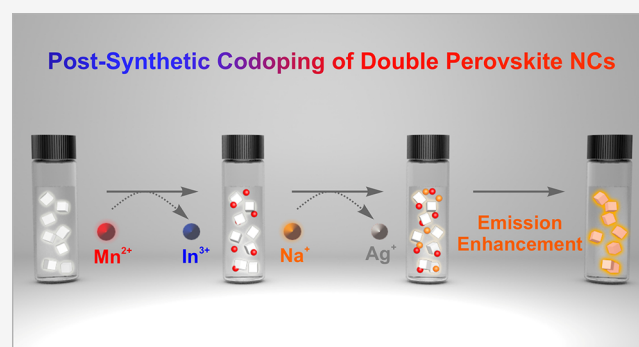
INTRODUCTION

Lead-free double perovskite nanocrystals (DP NCs, with a chemical formula of $Cs_2M(I)M(III)X_6$, where $M(I) = Ag^+$, Na^+, Cu^+, etc.; $M(III) = Bi^{3+}$, In^{3+}, Sb^{3+}, lanthanides, etc.; and $X = Cl^-$, Br^-, I^-) have attracted an extensive amount of research attention in recent years due to their reduced toxicity while maintaining a charge-neutral three-dimensional (3D) crystal structure with unique optoelectronic properties and enhanced stability.[1−4] The transition from a single, divalent, B-site metal (i.e., Pb^{2+}) in the conventional lead-halide perovskite to heterovalent dual B-sites (i.e., M(I) and M(III)) containing DP structure greatly expands compositional space and expedites the development of new perovskite materials.[5−11] In particular, $Cs_2AgInCl_6$ DP NCs possess a direct band gap and long photocarrier lifetimes with excellent light, thermal, and moisture stability, making them one of the most promising lead-free perovskite-type alternatives.[12−15] However, the low absorption extinction coefficient and weak, broad emission exhibited by the self-trapped excitons (STEs) of $Cs_2AgInCl_6$ DP NCs installed by the intrinsic parity-forbidden band gap transition significantly hinder their potential implementation into a wide variety of commercial applications.[13,16,17]

In this context, the doping of metal impurity ions into the DP crystal structure is one effective means to tune and enhance the physical and optoelectronic properties of the $Cs_2AgInCl_6$ DP NCs.[18−21] As such, reports indicate that the incorporation of transition metals (e.g., Cu^{2+}, Mn^{2+}) or lanthanide ions (e.g., Ce^{3+}, Tb^{3+}, Yb^{3+}) can modulate the band gap of the $Cs_2AgInCl_6$ DPs to exhibit additional strong and narrow absorption peaks in the visible light range or provide a more efficient radiative recombination pathway.[22−25] As one of the most studied systems, doping Mn^{2+} cations into $Cs_2AgInCl_6$ DP NCs can result in photoexcited energy transfer from the DP NC hosts to Mn^{2+} dopants, leading to a signature orange emission (~620 nm) through $d−d$ transitions (i.e., $^4T_{1g} \rightarrow ^6A_{1g}$) of the incorporated Mn^{2+} ion centers.[26−29] Such unique Mn-dopant-induced emission exhibits characteristic long
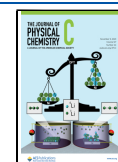
photoluminescence (PL) lifetimes, relatively high PL quantum yields (QYs), and large Stokes shifts with a minimized self-absorption behavior, which are all beneficial to applications including solid-state lighting, displays, or luminescence solar concentrators.[30−33]

Recently, we have developed a postsynthetic doping and transformation strategy to engineer and optimize presynthesized perovskite-type NCs in solid, liquid, or a combination of phases under ambient conditions.[32,34−37] Unlike direct synthetic reactions with fast reaction dynamics, the postsynthetic doping and transformation of perovskite NCs typically exhibit relatively slow kinetics with a stop-on-demand feature, allowing for detailed studies of composition−structure−property relationships of the materials.[34,35,38,39] For example, we previously reported a facile fabrication of Mn^{2+}-doped $CsPbCl_3$ perovskite NCs through a postsynthetic quasi-solid−solid cation exchange reaction in which the doping reaction occurred at the interface between the Mn-containing solid precursor and the surface of presynthesized $CsPbCl_3$ perovskite NCs. Enabled by this postsynthetic reaction, detailed doping mechanistic insights were obtained, demonstrating an initial surface doping reaction followed by a slow inward dopant diffusion process. Consequently, the dopant concentration/distribution and thus the optical properties of the resulting Mn^{2+}-doped $CsPbCl_3$ perovskite NCs can be precisely controlled and systemically optimized.[32,40]

In this work, we, for the first time, apply the postsynthetic doping strategy to a lead-free DP NC system. We investigate a liquid−solid cation exchange reaction that allows doping Mn^{2+} impurity ions into presynthesized $Cs_2AgInCl_6$ DP NCs. Similar to lead-halide perovskite NCs, an initial heterogeneous surface doping followed by a Mn-dopant inward diffusion reaction was observed and described. Moreover, given the versatility of the applied postsynthetic cation exchange reaction, we demonstrate that Na^+ ions can be concurrently doped with Mn^{2+} ions to not only aid the Mn-doping process but also enhance the PL QY of the resulting Na^+/Mn^{2+} codoped DP NCs by relaxing the intrinsic parity-forbidden electronic transition. Detailed studies on the doping mechanism, dopant-precursor, and NC ligand effect were carried out using various characterization techniques. Our studies presented here can not only shed light on the doping mechanism and dopant diffusion dynamics for both single-dopant and codopant systems but also highlight the impacts of surface ligand engineering on particle stabilization especially for lead-free perovskite-type NCs.

METHODS AND MATERIALS

Chemicals. The following reagents were used: cesium carbonate (Cs_2CO_3, Aldrich Chemicals, 99%), silver acetate (Ag(Ac), Acros Organics, 99.99%), indium(III) acetate ($In(Ac)_3$, Sigma-Aldrich, 99.99%), diphenyl ether (DPE, Alfa Aesar, 99.5%), oleic acid (OA, Sigma-Aldrich, 90%), oleylamine (OAm, Sigma-Aldrich, 70%), benzoyl chloride (Bz-Cl, Alfa Aesar, 98%), manganese(II) chloride tetrahydrate ($MnCl_2 \cdot 4H_2O$, Strem Chemicals, 98%), sodium carbonate (Na_2CO_3, Fisher Scientific, 99.8%), octanoic acid (Oct, Sigma-Aldrich, >98%). Hexanes and ethyl acetate were purchased from Fisher. Toluene-d_8 (D, 99.5%) was purchased from Cambridge Isotope Laboratories, Inc. All chemicals were used without further purification.

Syntheses. *Cesium Oleate.* To prepare a 0.5 M solution of cesium oleate, 0.4075 g (1.25 mmol) of Cs_2CO_3 was added to 5 mL of oleic acid in a three-necked round-bottomed flask.

The mixture was degassed under vacuum at room temperature for 1 h and then heated to 100 °C for another hour. Finally, the flask was heated to 150 °C under N_2 for 30 min until the solution was clear and slightly yellow.

Synthesis of $Cs_2AgInCl_6$ DP NCs. $Cs_2AgInCl_6$ DP NCs were synthesized following a modified literature method.[25] In a three-necked round-bottomed flask, 0.04 g (0.24 mmol) of Ag(Ac), 0.07 g (0.24 mmol) of $In(Ac)_3$, 1 mL of cesium oleate, 0.5 mL of OAm, and 4 mL of DPE were placed under vacuum at room temperature for 1 h and then subsequently heated to 40 °C for 30 min. Finally, the flask was heated to 105 °C under N_2. Once reaching 105 °C, a mixture of 200 μL of Bz-Cl and 500 μL of DPE was injected into the reaction flask. The reaction was swiftly quenched via cooling in an ice bath. The as-synthesized particles were centrifuged at 4500 rpm for 5 min and then redispersed in 10 mL of hexane.

Preparation of Mn-OAm Precursor. The Mn^{2+} precursor was prepared by adding 0.05 g (0.25 mmol) of finely ground $MnCl_2 \cdot 4H_2O$ salt to a glass vial containing 10 mL of hexane and 50 μL of OAm.[32] The solution was allowed to react for 24 h before the solution was purified by centrifugation and subsequent filtration.

Preparation of the Na-Oct Precursor. Sodium octanoate (Na-Oct) was synthesized using a modified procedure for preparing a cesium oleate solution. In detail, 0.132 g (2.5 mmol) of Na_2CO_3 was added to 500 μL of octanoic acid in a three-necked round-bottomed flask. The mixture was placed under vacuum at 70 °C for 1 h, and then the temperature was raised to 100 °C for another hour. Finally, the solution was heated to 120 °C under N_2 for 30 min before cooling to room temperature. The resultant solution was clear in color and was stored in a vial under ambient conditions. The same procedure was utilized for preparing the Na-Oct precursor with excess octanoic acid, but instead 5 mL of octanoic acid was used. In both cases, the as-prepared solution was further diluted in hexane to achieve the desired dopant concentration (0.1−0.5 mM).

Postsynthetic Cation Exchange. The particle concentration was kept consistent through excitonic peak normalization (optical density of 4.1 at 265 nm) via UV−vis absorption analysis. A postsynthetic Mn^{2+} doping reaction was conducted by adding 1.5 mL of Mn-OAm precursor solution to 2 mL of the as-synthesized $Cs_2AgInCl_6$ DP NCs hexane solution. The reaction was allowed to react for over 24 h, after which the particles were purified by adding in 0.5 mL of ethyl acetate to induce precipitation and then centrifuging at 4500 rpm for 5 min. The collected doped DP NCs were redispersed in 2 mL of hexane and aged for 5 days under ambient conditions. For the Na^+/Mn^{2+} codoping reaction, the reaction was carried out by adding 1.5 mL of Mn-OAm precursor solution and 0.5 mM of Na-Oct precursor to 2 mL of the as-synthesized $Cs_2AgInCl_6$ DP NCs hexane solution. The reaction was allowed to take place over 24 h without a further aging process, after which the particles were purified by addition to 0.5 mL of ethyl acetate to induce precipitation and then centrifuging at 4500 rpm for 5 min.

RESULTS AND DISCUSSION

Synthesis and Characterizations of Mn^{2+}-Doped $Cs_2AgInCl_6$ DP NCs through a Postsynthetic Reaction. Uniform $Cs_2AgInCl_6$ DP NCs with a cubic shape and an average edge length of 17.0 ± 1.9 nm were synthesized using a previously reported procedure.[12,25] Postsynthetic Mn^{2+} doping
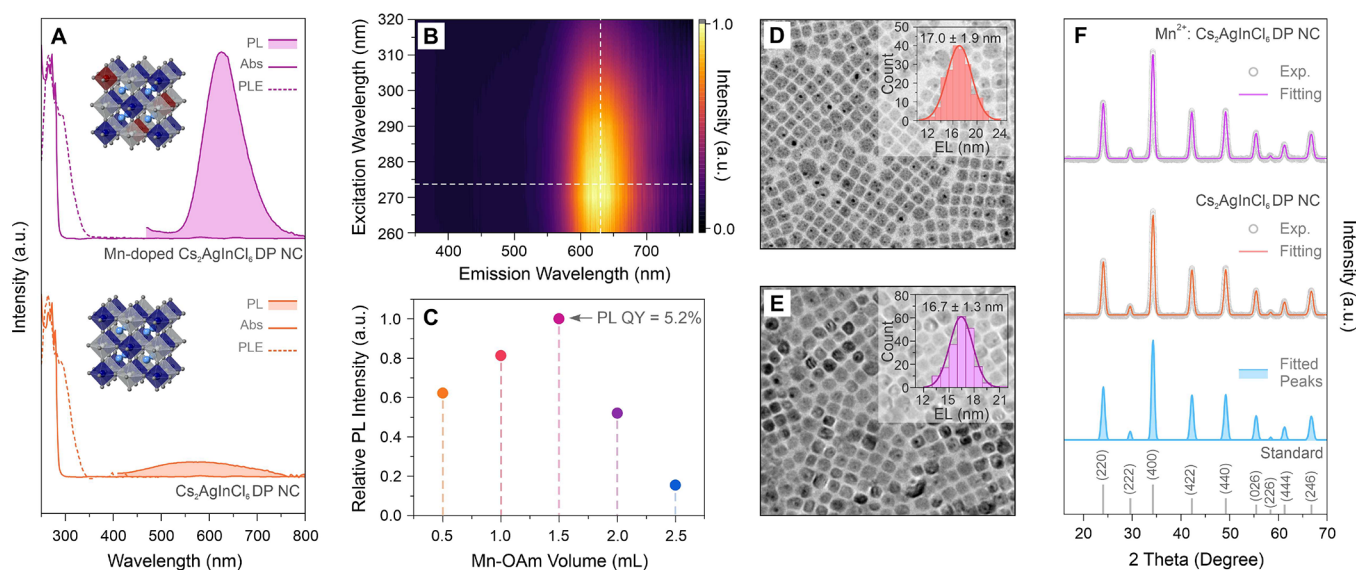
Figure 1. (A) Absorption spectra (solid lines), PLE spectra monitored at the strongest PL peak (dashed lines), and PL spectra (solid lines with shading) of the as-synthesized $Cs_2AgInCl_6$ DP NCs (orange) and Mn^{2+}-doped $Cs_2AgInCl_6$ DP NCs. (B) PL emission contour map of Mn^{2+}-doped $Cs_2AgInCl_6$ DP NCs. (C) Mn-OAm concentration-dependent PL intensity. (D, E) TEM images and size distribution histograms (insets) for the undoped (D) and Mn^{2+}-doped DP NCs (E). (F) XRD patterns (gray open circles) and fitted patterns (solid lines) for the as-synthesized $Cs_2AgInCl_6$ DP NCs (orange) and Mn^{2+}-doped $Cs_2AgInCl_6$ DP NCs (purple). Gray bars indicate the standard peak positions of bulk $Cs_2AgInCl_6$ DP. The constituent fitted XRD peaks are shown in light blue.

was achieved through a liquid−solid cation exchange reaction using an oleylamine (OAm)-ligand-activated $MnCl_2 \cdot 4H_2O$ precursor (denoted as Mn-OAm) (see details in the Methods and Materials). Briefly, the precursor−ligand interaction was initiated through the hydrogen bonds formed between the hydrated Mn^{2+} salt (i.e., $MnCl_2 \cdot 4H_2O$) and OAm, allowing Mn^{2+} dissolve into hexane.[32] The precursor solution was allowed to react for 24 h before purification to remove the undissolved solid precursor. The Mn-doping concentration in DP NCs was controlled through adjusting the volumetric ratios of the Mn-OAm precursor to a DP NC solution, and the postsynthetic Mn^{2+} doping reaction was accomplished in 24 h. After purification, the obtained Mn^{2+}-doped $Cs_2AgInCl_6$ DP NCs were further aged in hexane solution under ambient conditions for another 5 days to reach thermodynamic equilibrium.

The absorption spectra for both the undoped and Mn^{2+}-doped $Cs_2AgInCl_6$ DP NCs showed an absorption onset at around 300 nm. PL measurements showed that the as-synthesized $Cs_2AgInCl_6$ DP NC exhibited an STE broad band emission feature with a low PL QY of 1.2% (Figure 1A).[25] For the postsynthetic Mn^{2+} doping and aging processes, this STE emission feature was overshadowed by a characteristic Mn^{2+} emission peak (through $^4T_{1g}$ to $^6A_{1g}$ electronic transition) at 630 nm (Figure 1A), suggesting a successful doping of Mn^{2+} ions into the DP crystal structure.[25,29,32] The PL excitation (PLE) spectrum measured at the Mn^{2+} emission peak (i.e., 630 nm) overlapped well with the corresponding absorption profile of the DP NCs (Figure 1A), indicating an energy transfer process from the photogeneration exciton of the DP-NC to the excited electronic state (i.e., $^4T_{1g}$) of the Mn^{2+} centers in the Mn^{2+}-doped $Cs_2AgInCl_6$ DP NCs. The 2D emission contour map further highlighted the excitation-independent Mn PL, confirming the invariant radiative relaxation pathway through incorporated Mn^{2+} ion centers (Figure 1B).[32,33,41] Moreover, the utilization of liquid-based postsynthetic doping allows for

precise control of dopant concentration by adjusting the volumetric ratios of dopant precursor to the DP NC solution (see details in the SI). An initial positive correlation between the Mn-dopant concentration and PL intensity was observed (Figure 1C). Such an Mn PL intensity increase was attributed to the incorporation of an increased number of Mn-emission centers in the DP NCs,[25] as confirmed by inductively coupled plasma-atomic emission spectroscopy (ICP-AES) measurements (Table S1). A maximum PL QY of 5.2% (Table S2) was achieved at the Mn doping concentration of 0.2% (Mn doping concentration = $[Mn]/([In] + [Mn])$). After the initial increase, a subsequent PL intensity drop was obtained when further increasing the Mn dopant concentration (>0.2%) in the DP NCs, while the structure was determined to remain intact. In contrast, the introduction of excess OAm while adding any more Mn dopant precursor (i.e., 2.5 mL) caused additional PL quenching and DP NC decomposition through AgCl extraction (Figure S1, Table S3).[42]

Transmission electron microscopy (TEM) measurements and X-ray diffraction (XRD) characterizations were carried out to confirm the morphology and structural integrity of the DP NCs following the postsynthetic Mn-doping reaction and the subsequent aging process. These characterizations were performed by utilizing 1.5 mL of Mn-OAm due to the optimal optical properties and dopant incorporation. The samples both before and after postsynthetic Mn^{2+} incorporation showed uniform DP NCs with a cubic shape with a nearly unchanged edge length of ~17 nm (Figure 1D,E). The unchanged crystal structure of the DP NCs was confirmed by the XRD measurements, which consistently showed the intact DP crystal phase for the as-synthesized $Cs_2AgInCl_6$ DP NC (Figure S2, Table S3) as well as the final Mn^{2+}-doped $Cs_2AgInCl_6$ DP NCs after aging (Figure 1F, Table S4). No clear lattice contraction of the DP NCs after doping was observed, which was attributed to the low dopant concentration (i.e., 0.2%) of the sample.[29]

PL measurements showed that immediately following the postsynthetic doping reaction (before the aging process), the Mn-emission peak was observed to be at 660 nm, redder than the typical Mn-emission peak range of 590−620 nm, indicating the DP NCs with inhomogeneous surface-doped Mn^{2+} ions.[29,31,43] The Mn-emission peak then blue-shifted from 660 to 630 nm during the subsequent aging process, implying an internalization of Mn^{2+} cations through an entropy-driven inward diffusion process as previously reported for the Mn^{2+}-doped $CsPbCl_3$ perovskite NCs (Figure 2A,B).[32] The onsite
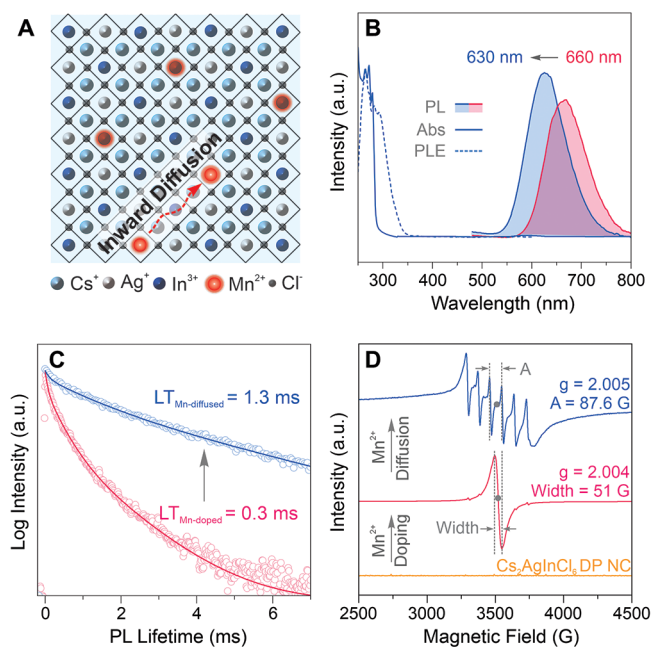

Figure 2. (A) Schematic representation of the Mn^{2+} surface dopants undergoing inward diffusion. (B) Absorption spectrum (blue solid line), PLE spectrum monitored at the strongest PL peak (blue dashed line) and PL spectra (solid lines with shading) of the Mn^{2+} doped $Cs_2AgInCl_6$ DP NCs before (pink) and after (blue) Mn-dopant inward diffusion. 1.5 mL of Mn-OAm precursor solution was utilized for the postsynthetic doping reaction. (C) PL lifetime (LT) plots (open circles) and fitted curves (solid lines) of the Mn^{2+}-doped $Cs_2AgInCl_6$ DP NCs before (pink) and after (blue) Mn-dopant inward diffusion. (D) EPR spectra of the as-synthesized $Cs_2AgInCl_6$ DP NCs (orange), and the Mn^{2+}-doped $Cs_2AgInCl_6$ DP NCs before (pink) and after (blue) Mn-dopant inward diffusion. The g factors are determined using the peak center marked with gray dots.

Mn^{2+} inward diffusion process was further confirmed by time-resolved PL spectroscopy measurements (Figure 2C). The Mn-emission PL lifetime was prolonged from 0.2 ms for the initial surface Mn^{2+}-doped DP NCs to 1.2 ms for the aged DP NCs with internalized Mn^{2+} cation centers. (Note: The PL lifetime for the undoped $Cs_2AgInCl_6$ DP NCs was reported to be 6 μs.[44]) The significantly prolonged Mn-dopant emission lifetime (Figure S3, Table S5) was attributed to both the weakened Mn−Mn coupling interaction and the installation of the centrosymmetric octahedral symmetry of the individual Mn^{2+} ion centers (enforcing the Laporte selection rule for the electronic transition of $^4T_{1g} \rightarrow {}^6A_{1g}$) upon inward diffusion.[30,44,45] Furthermore, the presence of Mn^{2+} ion centers and its inward diffusion were also confirmed via electron paramagnetic resonance (EPR) measurements. After doping Mn^{2+} ions into the DP lattice, a single broadband EPR feature

emerged with a peak width of 51 G and a g value of 2.004 (Figure 2D). Such a broad EPR signal is a characteristic feature of the inhomogeneous Mn^{2+} ions doped on the NC surface with incomplete coordination environments and strong Mn−Mn exchange coupling interactions,[30,32] in good accordance with the optical measurement results. After the Mn^{2+}-doped DP NCs were aged in solution for 5 days, the single EPR peak turned into a sextet hyperfine splitting pattern with a coupling constant of 87.6 G and a g value of 2.005 (Figure 2D), signifying the dispersed Mn^{2+} ions located in an octahedral coordination environment (i.e., $[MnCl_6]^{4-}$ octahedral subunits) in the DP lattice (Figure S4).[33,46] Together, all of these results unambiguously proved the initial inhomogeneous surface Mn^{2+} doping followed by an onsite dopant inward diffusion process for the postsynthetic reaction of Mn^{2+} doping into $Cs_2AgInCl_6$ DP NCs.

Postsynthetic Synthesis of Na^+/Mn^{2+} Codoped $Cs_2AgInCl_6$ DP NCs. Codoping more than one type of cation into DP NCs has garnered significant attention recently due to the potential optoelectronic property enhancements that can be achieved.[43,47,48] In particular, recent studies have demonstrated that Na^+ doping into DP NCs can improve the stability of the materials by raising the energetic barrier for halide vacancy diffusion and can enhance the PL through breaking the symmetry of octahedral sublattice units and reducing the density of surface trap states.[41,49,50] To evaluate the Na^+ doping effect in our system, we expanded our postsynthetic strategy to codoping Na^+ and Mn^{2+} cations into the $Cs_2AgInCl_6$ DP NCs.

Sodium octanoate (Na-Oct) liquid-based precursor was prepared through the modification of a previously reported procedure in which sodium carbonate was reacted with octanoic acid stoichiometrically to produce a clear, light-yellow precursor solution (see details in the Methods and Materials).[51] Then, a fixed volume (i.e., 100 μL) of the as-prepared Na-Oct precursor solution with varied concentration (0.1−0.5 mM) and a fixed amount of Mn-OAm precursor (i.e., 1.5 mL) were simultaneously introduced into the DP NC hexane solution for a 24 h postsynthetic doping reaction. Figure 3A shows the concentration-dependent PL enhancement following the introduction of dopant precursor solutions. Unlike the Mn-only doping reaction, the Mn-emission peak emerged at 630 nm after the 24 h reaction on top of a broad emission feature (Figure 3A). This broad emission can be assigned to the inherent $Cs_2AgInCl_6$ DP NC STE emission, which was enhanced by the reduction in electronic dimensionality imposed by Na^+ incorporation and thus partial isolation of the Jahn−Teller distorted $[AgCl_6]^{5-}$ octahedral subunits.[52,53] Both the PLE spectra and 2D PL contour map of the Na^+/Mn^{2+} codoped $Cs_2AgInCl_6$ DP NCs showed a slight blue shift in the excitation to 255 nm (Figure 3A,B) upon Na^+ incorporation, which is in agreement with the literature.[29] In contrast to the unchanged absorbance features when achieving the Mn^{2+}-doped DP NCs, the Na^+/Mn^{2+}-codoped DP NCs' absorption profile exhibits a strong blue shift with a broadening effect that leads to a long absorption tail in correspondence to the volume defect trapping (Figure S5).[29] Additionally, a similar peak blue-shifting effect was also observed in the PLE spectrum measurement upon increasing the added Na-Oct precursor concentration (Figure S6).[29,54] Negligible optical property changes were observed upon further aging the sample for another 5 days, indicating that no subsequent Mn-dopant inward diffusion occurred as for the Mn-only doped sample.
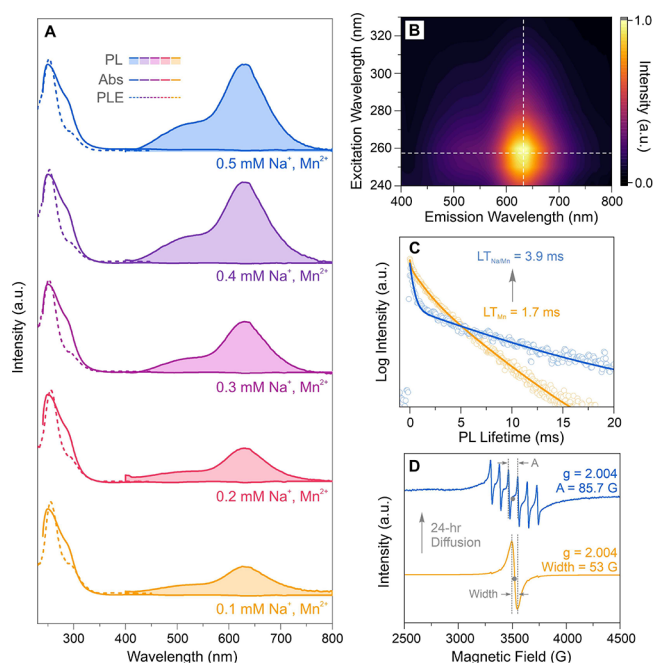
Figure 3. (A) Absorption spectra (solid lines), PLE spectra monitored at the strongest PL peak (dashed lines), and PL spectra (solid lines with shading) upon varying the concentration of the added Na-Oct precursor for the Na^+/Mn^{2+} codoped $Cs_2AgInCl_6$ DP NCs. (B) PL emission contour map of the Na^+/Mn^{2+} codoped $Cs_2AgInCl_6$ DP NCs. (C) PL LT plots (open circles) and fitted curves (solid lines) of the Na^+/Mn^{2+} codoped $Cs_2AgInCl_6$ DP NCs before (orange) and after (blue) dopant inward diffusion. (D) EPR spectra of the Na^+/Mn^{2+} codoped $Cs_2AgInCl_6$ DP NCs before (orange) and after (blue) dopant inward diffusion.

These results suggested that codoping Na^+ ions can accelerate the dopant diffusion dynamics to allow reaching homogeneous Mn^{2+} doping equilibrium within a 24 h reaction time (vs 5

days for the Mn-only doped case). Such fast Mn-dopant diffusion was further confirmed by the EPR measurements where a single Mn−Mn coupling peak was exhibited in the Na^+/Mn^{2+} codoped DP NC sample after only 1 h of postsynthetic reaction (Figure 3D). The sextet hyperfine splitting pattern (g = 2.004, A = 85.7 G) emerged for the as-synthesized Na^+/Mn^{2+} codoped DP NCs after a 24 h reaction (Figure 3D). In addition, although the feeding amount of the Mn-precursor solution (i.e., 1.5 mL) was kept consistent for all of the reactions, ICP-AES analysis showed that the Mn-dopant concentration increased from 0.2 to 0.5% when increasing the concentration of the added Na-Oct precursor solution from 0.1 to 0.5 mM (Table S1). X-ray photoelectron spectroscopy (XPS) and scanning TEM energy dispersive spectroscopy (EDS) measurements determined a maximum Na-dopant concentration of 2.0% (Tables S6 and S7). The highest PL QY of 7.1% was achieved when the concentration of the added Na-Oct solution reached 0.5 mM (Table S8), suggesting a 37% enhancement in PL QY as compared to that of the Mn-only doped DP NCs through the postsynthetic doping reaction. The PL lifetime of the sample was prolonged to 3.9 ms with the emergence of a short PL lifetime component, which can be attributed to lattice defect trapping effects (Figure 3C, Figure S7, and Table S9). Further increasing the Na-Oct precursor concentration resulted in the DP NC degradation (Figure S8, Table S10), likely due to the presence of an excess amount of negatively charged carboxylate.[55] In all, these results indicated that codoping with Na^+ ions results in faster Mn-dopant diffusion dynamics and also promoted Mn^{2+} doping to the $Cs_2AgInCl_6$ DP NCs with enhanced optical properties.

Tuning Optical Properties through Surface Engineering of Na^+/Mn^{2+} Codoped $Cs_2AgInCl_6$ DP NCs. Previous studies have shown how the surface state of $CsPbX_3$ lead-halide perovskite NCs influences the postsynthetic doping and transformation processes, such as regulating the physical, optical, and magnetic properties of the final NCs.[56,57]
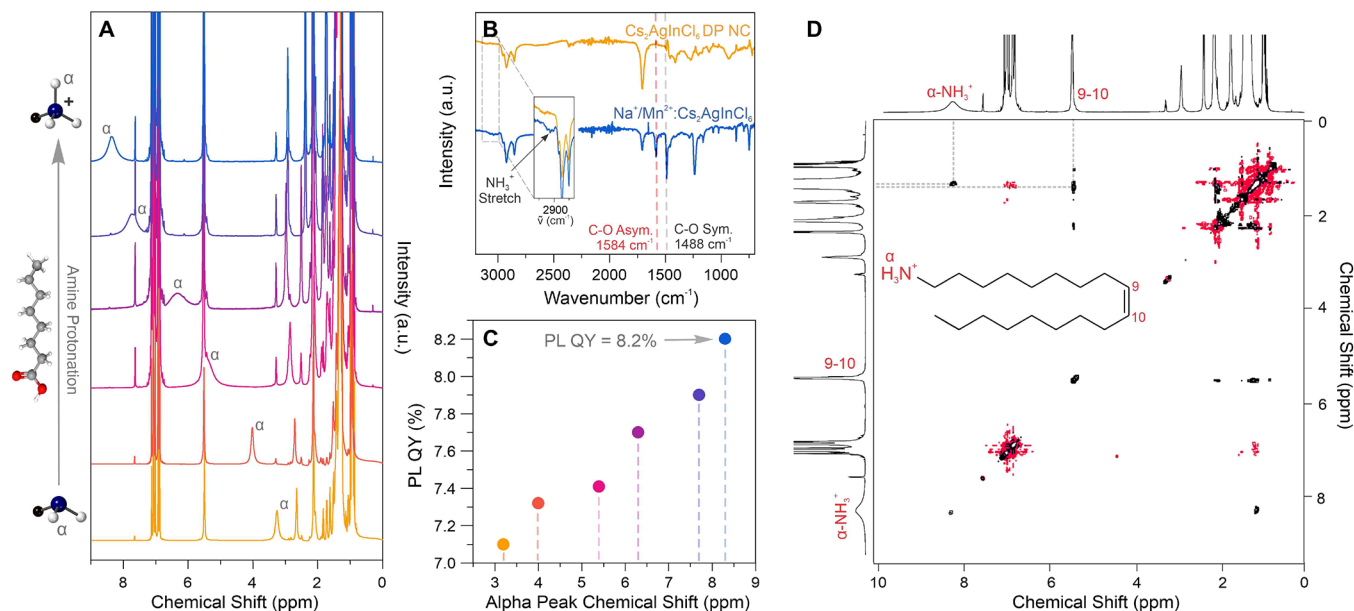

Figure 4. (A) ^1H NMR spectra of the Na^+/Mn^{2+} codoped $Cs_2AgInCl_6$ DP NC solutions following the protonation of OAm (bottom) to form oleylammonium (top). (B) FTIR spectra of the as-synthesized $Cs_2AgInCl_6$ DP NCs (orange) and Na^+/Mn^{2+} codoped $Cs_2AgInCl_6$ DP NCs (blue). (C) Correlated PL QY increased with the increased level of OAm protonation (oleylammonium formation). (D) 2D-NOESY spectrum of the Na^+/Mn^{2+} codoped $Cs_2AgInCl_6$ DP NCs. The black and red signals represent the positive and negative cross-relaxation rates, respectively.

However, few publications carry out in-depth surface and ligand state analyses of lead-free perovskite NC analogues. Here, we conducted detailed studies on the surface states of the lead-free DP NCs through NMR spectroscopic measurements to provide insights into the correlation between postsynthetic doping processes and surface states as well as ligand binding/diffusion dynamics of the DP NCs in our system.

^{1}H NMR analysis confirmed the presence of OAm capping ligands on the surface of the as-synthesized $Cs_2AgInCl_6$ DP NCs (Figure S9), with a characteristic broadening effect for the NMR peak (at 3.2 ppm) of the bound α-hydrogens (denoted as the α-peak) on the amine group (Figure 4A). As reported previously, this characteristic α-peak is highly sensitive to the protonation level of the OAm ligand bound to the particle surface.[32] This upfield-shifted α-peak position at 3.2 ppm indicated that the unprotonated OAm served as the major surface ligand on the DP NCs, consistent with the effective removal of oleate capping ligands during the NC purification process.[32,58] The addition of the Mn-OAm precursor (with additional unprotonated amine) resulted in no further shifting of the α-peak (Figure S9). In contrast, the α-peak gradually shifted downfield from 3.2 to 8.3 ppm when increasing the concentration of the added Na-Oct precursor from 0.1 to 0.5 mM in the codoping reaction (Figure 4A). This was due to the acid−base-driven formation of oleylammonium (i.e., amine protonation process[56]) caused by the added Na-Oct precursor containing excess free octanoic acid (Figure S11, Table S11). Concurrently, the width of the α-peak (expressed at the full width at half-maximum, fwhm) expanded from ~80 to ~260 Hz (Figure 4A). This α-peak broadening effect implies that the positively charged oleylammonium species exhibit slower tumbling dynamics than the unprotonated OAm when bound to the DP NC surface, indicating a higher binding affinity of oleylammonium to the NC surface.[58] The DP NC surface ligands were also probed by Fourier transform infrared (FTIR) spectroscopy measurements. As shown in Figure 4B, the as-synthesized $Cs_2AgInCl_6$ DP NCs exhibited the presence of unprotonated OAm ligands as well as free oleate (peak at 1710 cm^{-1}), which disappeared after the purification and the subsequent Mn-OAm postsynthetic doping (Figure S12, Table S12). In contrast, when utilizing the Na^+/Mn^{2+} postsynthetic codoping method and subsequent purification, the DP NCs exhibited the bound octanoate asymmetric and symmetric C−O stretching peaks at 1584 and 1488 cm^{-1}, respectively, as well as the C=O vibrational peak at 1709 cm^{-1} (Figure 4B). Additionally, the appearance of N−H stretching of NH_3^+ at 3100 cm^{-1} proved the generation of oleylammonium through the OAm protonation and the subsequent surface ligand coordination of the codoped NCs.[32,59,60] These FTIR results confirmed that the DP NCs were mainly terminated by octanoate and oleylammonium ligands.

Interestingly, a PL intensity increasing trend was observed along with the increased level of amine protonation, which ultimately resulted in the highest PL QY of 8.2% at a Mn doping concentration of 0.5% (Figure 4C). We previously reported an opposite trend of PL intensity change when doping Mn^{2+} ions into $CsPbCl_3$ perovskite NCs by adding carboxylate acid (i.e., tuning the protonation level of amine ligands) to control the degree of the Mn-precursor activation.[32] However, in this case, the Mn-OAm precursor was premade before mixing with the Na-Oct precursor that contained free octanoic acid. Therefore, the octanoic acid,

instead of hindering the Mn-precursor activation,[32] played a minimal role in the precursor activation process. As a result, the PL enhancement trend observed here should be explained by two reasons: the Na-induced symmetry-breaking effect and the Mn-doping concentration increase caused by codoping with Na^+ ions as discussed above. Moreover, the oleylammonium molecules generated during the amine-protonation process in the codoping reaction can serve as effective ligands and substituent species to passivate undercoordinated Cl^- sites and Cs^+ vacancies on the DP NC surfaces, respectively.[58,61]

To further confirm the ligand passivation mechanism, in-depth 2D NMR analyses were performed utilizing nuclear Overhauser effect spectroscopy (NOESY) and diffusion ordered spectroscopy (DOSY). NOESY is an NMR technique that offers a view of through-space interactions, which is particularly useful for gaining insight into the bonding mode of ligands on the NC surface. When compared to the free ligand molecules, the ligand species that are bound to the NC surface exhibit a prominent and positive cross-relaxation rate. This is reflected as a positive cross peak (in relation to the diagonal peaks) in the 2D NOESY spectrum.[61−63] In the NOESY spectrum of the Na^+/Mn^{2+} codoped DP NC sample, distinctive bonding peaks emerged, which can be assigned to the α-hydrogens of the amine group (the α-peak at 8.2 ppm) and the hydrogens on the double bond (the peak at 7.1 ppm) of the alkene carbon chains in the ligands (Figure 4D). It is worth noting that both of these bonding modes have been previously reported as potential interactions for oleylamine/ammonium species.[61,64] Taken together with the discussed α-peak broadening effect, these findings suggest a higher NC surface binding affinity of oleylammonium as compared to OAm. Such enhanced binding can be achieved by occupying the surface Cs^+/Ag^+ vacancies and passivating uncoordinated surface Cl^- sites of the DP NCs, in line with previous reports for similar systems.[58,61]

To further prove this ligand passivation effect, the 2D DOSY NMR technique was employed to provide a quantitative confirmation of the enhanced ligand binding affinity. DOSY utilizes magnetic field pulse gradients to acquire spatial information about molecules in a solution. This information can then be utilized to deduce the corresponding diffusion coefficients of different molecular species.[65] Free ligands typically exhibit a higher diffusion coefficient in comparison with those ligands that are bound to NC surfaces. Ligands that are weakly bound to the NC surfaces are more prone to undergo ligand exchange interactions with the surrounding free ligands in the solution, which can also affect the measured diffusion coefficients.[63,66−68] For direct comparison, three sets of samples were used for DOSY NMR measurements using toluene-d_8 as the solvent: free ligands (i.e., oleylamine and oleylammonium) to establish baseline diffusion coefficients; as-synthesized $Cs_2AgInCl_6$ DP NCs passivated with unprotonated OAm ligands; and Na^+/Mn^{2+} codoped DP NCs passivated by protonated oleylammonium ligands (Figures S13−S15). The DOSY NMR results revealed a significant reduction in the diffusion coefficient of the bound OAm ligands on the as-synthesized DP NCs with a value of 5.9×10^{-11} m^2 s^{-1}, in comparison to the free OAm molecules, which exhibited a diffusion coefficient of 1.0×10^{-9} m^2 s^{-1} (Table S13). Moreover, for the Na^+/Mn^{2+} codoped DP NC sample, the diffusion coefficient of the surface-bound oleylammonium ligands was further reduced to 2.2×10^{-12} m^2 s^{-1}. This lower value indicated an increased binding affinity to the DP NC
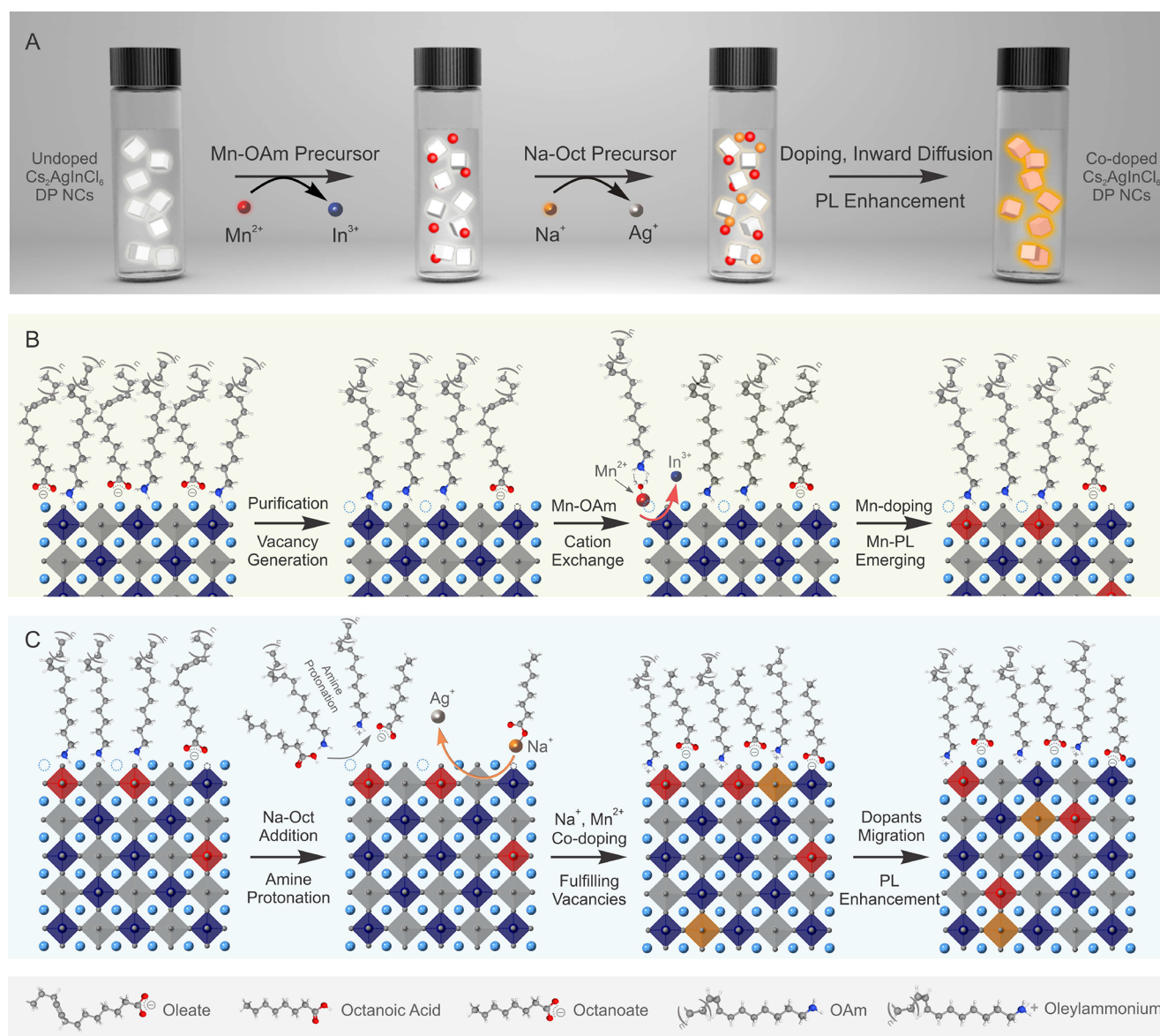
Figure 5. (A) Schematic illustration of the experimental process for post-synthetic doping to $Cs_2AgInCl_6$ DP NCs. (B) Purification and subsequent ligand-mediated Mn^{2+} cation doping mechanism. (C) Na^+ cation exchange mechanism, oleylammonium formation, and inward diffusion of the $Cs_2AgInCl_6$ DP NCs.

surface when comparing the unprotonated OAm to the protonated oleylammonium ligands, consistent with the NOESY NMR results. Collectively, these 2D NMR spectroscopic results harmonized well with the optical data discussed earlier, aligning with previously reported trends for perovskite-type NCs capped with amine-based ligands.[67,69,70]

Underlining Mechanism of the Postsynthetic Doping Reaction. The overall postsynthetic doping process is summarized and illustrated in Figure 5A. The as-synthesized $Cs_2AgInCl_6$ DP NCs exhibit a CsCl surface termination with OAm and oleate capping ligands (Figure 5B, leftmost).[61,71] As noted by Manna et al.,[56] perovskite NCs often form defects within the crystal lattice structure, which then migrate to the particle surface after the synthesis and subsequent purification process. Specifically for $Cs_2AgInCl_6$ DP NCs, the CsCl surface termination commonly leads to the thermodynamically favored formation of Cs^+ and Cl^- vacancies rather than disrupting the structural integrity of internal metal halide octahedra units (i.e.,

$[InCl_6]^{3-}$ or $[AgCl_6]^{5-}$ octahedra.[72] Moreover, the rigorous purification process effectively removes the majority of negatively charged oleate ligands, thereby leaving Cs^+ vacancies on the particle surfaces (Figure 5B, middle left). This process results in OAm remaining as the primary binding ligands on the NC surfaces,[55] which has been confirmed by the FTIR spectroscopic measurements (Figure 4B, Figure S12). While these surface defect states impose limitations on the initial DP NCs' optical performance, they provide readily accessible cation exchange sites (i.e., the exposed metal-chloride octahedra with relatively weak OAm passivation) for postsynthetic doping reactions to occur (Figure 5B, middle right).[73] Consequently, upon the introduction of the Mn-OAm precursor, a facile cation exchange between In^{3+} and Mn^{2+} takes place, leading to the production of Mn^{2+} surface-doped DP NCs.[74] The excess number of OAm ligands in the reaction solution allows for immediate ligand passivation and substitution, and thus the doping process is achieved without

any loss of ligands or disruption to the DP crystal lattices (Figure 5B, rightmost).

Upon adding Na-Oct precursor during the codoping reaction (Figure 5C), the free octanoic acid in the Na-Oct precursor initiates an acid−base reaction with the OAm (introduced via adding the Mn-OAm precursor). This reaction yields oleylammonium and octanoate species (Figure 5C, middle left), both of which are effective in passivating the NC surfaces. Besides, the produced oleylammonium can balance the surface charge discrepancy generated by the dynamic postsynthetic Mn^{2+} doping process (replacing In^{3+} cations). Meanwhile, the excess negatively charged octanoate species promote vacancy-driven metal-site doping by extracting the surface-exposed metal cations (Ag^+ and In^{3+} ions) (Figure 5C, middle left).[73,75] This mechanism not only facilitates the Ag^+-to-Na^+ cation exchange for doping Na^+ ions but also promotes the Mn^{2+} doping by enhancing the physical and electronic flexibility of the atomic configurations on the DP NC surfaces. Such a Mn^{2+} doping facilitation effect was supported by the experimental observation of the increased Mn^{2+} doping concentration when codoping with Na^+ ions (Tables S1, S6, and S7). Throughout this exchange reaction, the positively charged oleylammonium species can not only bind ionically to the surface-terminated Cl^- sites but also fill the surface Cs^+ vacancies. Meanwhile, the negatively charged octanoate ligands stabilize the remaining surface-exposed Cs^+ sites and possibly fill Cl^- vacancies (Figure 5C, middle right). Moreover, the coexistence of short (i.e., octanoate) and long (i.e., oleylammonium) carbon-chain ligands on the DP NC surfaces mitigates the overall steric hindrance imposed by the capping ligands. This, in turn, increases the ligand density and enhances particle stability.[76] Finally, the aging process of the Na^+/Mn^{2+} codoped $Cs_2AgInCl_6$ DP NCs allows for the dopant internalization from the particle surface until reaching the ultimate thermodynamic equilibrium (Figure 5C, rightmost).

CONCLUSIONS

Our study provides a comprehensive exploration of the postsynthetic doping and codoping processes involving Mn^{2+} and Na^+ ions within lead-free $Cs_2AgInCl_6$ DP NCs. Through the incorporation of Mn^{2+} ions via a liquid−solid cation exchange reaction followed by gradual dopant inward diffusion, Mn^{2+}-doped $Cs_2AgInCl_6$ DP NCs are successfully engineered, achieving a peak PL QY of 5.2%. The additional codoping of Na^+ ions results in the further enhancement in PL QY, driven by the relaxation of parity-forbidden transitions and the effective passivation of surface defects during the codoping reaction. Our investigation delves into the intricate passivation mechanisms involving oleylammonium and octanoate ligands on the DP NC surfaces, shedding light on the ligand-mediated metal cation doping process. This study not only advances the comprehension of postsynthetic doping and codoping mechanisms in lead-free perovskite NCs but also introduces a novel avenue for tailoring their optical and optoelectronic properties. These insights enrich the evolving landscape of perovskite nanomaterials, offering new possibilities for their utilization in a diverse array of optoelectronic applications, including photovoltaics, light-emitting devices, sensors, and displays.

ASSOCIATED CONTENT

ⓢ Supporting Information

The Supporting Information is available free of charge at https://pubs.acs.org/doi/10.1021/acs.jpcc.3c05901.

Experiment, characterization and fitting details, and additional UV−vis absorption, PL, PL lifetime, XRD, EPR, NMR, FITR, ICP-AES, and STEM-EDS data (PDF)

AUTHOR INFORMATION

Corresponding Author

Ou Chen − *Department of Chemistry, Brown University, Providence, Rhode Island 02912, United States;* ⓞ orcid.org/0000-0003-0551-090X; Email: ouchen@brown.edu

Authors

Lacie Dube − *Department of Chemistry, Brown University, Providence, Rhode Island 02912, United States*

Peter Saghy − *Department of Chemistry, Brown University, Providence, Rhode Island 02912, United States*

Complete contact information is available at:
https://pubs.acs.org/10.1021/acs.jpcc.3c05901

Author Contributions

L.D. and O.C. conceptualized the project. L.D. conducted sample preparations, characterization measurements, and data analysis. P.S. helped with data analysis. O.C. supervised the project.

Notes

The authors declare no competing financial interest.

REFERENCES

(1) Maughan, A. E.; Ganose, A. M.; Scanlon, D. O.; Neilson, J. R. Perspectives and Design Principles of Vacancy-Ordered Double Perovskite Halide Semiconductors. *Chem. Mater.* **2019**, *31* (4), 1184−1195.

(2) Luo, J.; Hu, M.; Niu, G.; Tang, J. Lead-Free Halide Perovskites and Perovskite Variants as Phosphors toward Light-Emitting Applications. *ACS Appl. Mater. Interfaces* **2019**, *11* (35), 31575−31584.

(3) Wang, Y.; Song, L.; Chen, Y.; Huang, W. Emerging New-Generation Photodetectors Based on Low-Dimensional Halide Perovskites. *ACS Photonics* **2020**, *7* (1), 10−28.

(4) Saghy, P.; Brown, A. M.; Chu, C.; Dube, L. C.; Zheng, W.; Robinson, J. R.; Chen, O. Lanthanide Double Perovskite Nanocrystals with Emissions Covering the UV-C to NIR Spectral Range. *Advanced Optical Materials* **2023**, *11* (12), No. 2300277.

(5) Chakraborty, S.; Xie, W.; Mathews, N.; Sherburne, M.; Ahuja, R.; Asta, M.; Mhaisalkar, S. G. Rational Design: A High-Throughput Computational Screening and Experimental Validation Methodology for Lead-Free and Emergent Hybrid Perovskites. *ACS Energy Letters* **2017**, *2* (4), 837−845.

(6) Jena, A. K.; Kulkarni, A.; Miyasaka, T. Halide Perovskite Photovoltaics: Background, Status, and Future Prospects. *Chem. Rev.* **2019**, *119* (5), 3036−3103.

(7) Utzat, H.; Sun, W.; Kaplan, A. E. K.; Krieg, F.; Ginterseder, M.; Spokoyny, B.; Klein, N. D.; Shulenberger, K. E.; Perkinson, C. F.; Kovalenko, M. V.; et al. Coherent single-photon emission from colloidal lead halide perovskite quantum dots. *Science* **2019**, *363* (6431), 1068−1072.

(8) Kovalenko, M. V.; Protesescu, L.; Bodnarchuk, M. I. Properties and potential optoelectronic applications of lead halide perovskite nanocrystals. *Science* **2017**, *358* (6364), 745−750.

(9) Nedelcu, G.; Protesescu, L.; Yakunin, S.; Bodnarchuk, M. I.; Grotevent, M. J.; Kovalenko, M. V. Fast Anion-Exchange in Highly Luminescent Nanocrystals of Cesium Lead Halide Perovskites ($CsPbX_3$, X = Cl, Br, I). *Nano Lett.* **2015**, *15* (8), 5635−5640.

(10) Cai, T.; Shi, W.; Hwang, S.; Kobbekaduwa, K.; Nagaoka, Y.; Yang, H.; Hills-Kimball, K.; Zhu, H.; Wang, J.; Wang, Z.; et al. Lead-Free $Cs_4CuSb_2Cl_{12}$ Layered Double Perovskite Nanocrystals. *J. Am. Chem. Soc.* **2020**, *142* (27), 11927−11936.

(11) Liu, Z.; Yang, H.; Wang, J.; Yuan, Y.; Hills-Kimball, K.; Cai, T.; Wang, P.; Tang, A.; Chen, O. Synthesis of Lead-Free Cs_2AgBiX_6 (X = Cl, Br, I) Double Perovskite Nanoplatelets and Their Application in CO_2 Photocatalytic Reduction. *Nano Lett.* **2021**, *21* (4), 1620−1627.

(12) Liu, Y.; Nag, A.; Manna, L.; Xia, Z. Lead-Free Double Perovskite $Cs_2AgInCl_6$. *Angew. Chem.* **2021**, *133* (21), 11696−11707.

(13) Lee, W.; Hong, S.; Kim, S. Colloidal Synthesis of Lead-Free Silver−Indium Double-Perovskite $Cs_2AgInCl_6$ Nanocrystals and Their Doping with Lanthanide Ions. *J. Phys. Chem. C* **2019**, *123* (4), 2665−2672.

(14) Liao, Q.; Meng, Q.; Jing, L.; Pang, J.; Pang, Q.; Zhang, J. Z. Highly Emissive and Stable $Cs_2AgInCl_6$ Double Perovskite Nanocrystals by Bi^{3+} Doping and Potassium Bromide Surface Passivation. *J. Phys. Chem. C* **2021**, *125* (33), 18372−18379.

(15) Protesescu, L.; Yakunin, S.; Bodnarchuk, M. I.; Krieg, F.; Caputo, R.; Hendon, C. H.; Yang, R. X.; Walsh, A.; Kovalenko, M. V. Nanocrystals of Cesium Lead Halide Perovskites ($CsPbX_3$, X = Cl, Br, and I): Novel Optoelectronic Materials Showing Bright Emission with Wide Color Gamut. *Nano Lett.* **2015**, *15* (6), 3692−3696.

(16) Liu, Y.; Jing, Y.; Zhao, J.; Liu, Q.; Xia, Z. Design Optimization of Lead-Free Perovskite $Cs_2AgInCl_6$:Bi Nanocrystals with 11.4% Photoluminescence Quantum Yield. *Chem. Mater.* **2019**, *31* (9), 3333−3339.

(17) Luo, J.; Li, S.; Wu, H.; Zhou, Y.; Li, Y.; Liu, J.; Li, J.; Li, K.; Yi, F.; Niu, G.; et al. $Cs_2AgInCl_6$ Double Perovskite Single Crystals: Parity Forbidden Transitions and Their Application For Sensitive and Fast UV Photodetectors. *ACS Photonics* **2018**, *5* (2), 398−405.

(18) Han, P.; Han, K. Recent Advances in All-Inorganic Lead-Free Three-Dimensional Halide Double Perovskite Nanocrystals. *Energy Fuels* **2021**, *35* (23), 18871−18887.

(19) Liu, Y.; Rong, X.; Li, M.; Molokeev, M. S.; Zhao, J.; Xia, Z. Incorporating Rare-Earth Terbium(III) Ions into $Cs_2AgInCl_6$:Bi Nanocrystals toward Tunable Photoluminescence. *Angew. Chem., Int. Ed.* **2020**, *59* (28), 11634−11640.

(20) Arfin, H.; Kaur, J.; Sheikh, T.; Chakraborty, S.; Nag, A. Bi^{3+}-Er^{3+} and Bi^{3+}-Yb^{3+} Codoped $Cs_2AgInCl_6$ Double Perovskite Near-Infrared Emitters. *Angew. Chem., Int. Ed.* **2020**, *59* (28), 11307−11311.

(21) Zhang, A.; Liu, Y.; Liu, G.; Xia, Z. Dopant and Compositional Modulation Triggered Broadband and Tunable Near-Infrared Emission in $Cs_2Ag_{1-x}Na_xInCl_6$:Cr^{3+} Nanocrystals. *Chem. Mater.* **2022**, *34* (7), 3006−3012.

(22) Liao, Q.; Chen, J.; Zhou, L.; Wei, T.; Zhang, L.; Chen, D.; Huang, F.; Pang, Q.; Zhang, J. Z. Bandgap Engineering of Lead-Free Double Perovskite $Cs_2AgInCl_6$ Nanocrystals via Cu^{2+}-Doping. *J. Phys. Chem. Lett.* **2020**, *11* (19), 8392−8398.

(23) Mahor, Y.; Mir, W. J.; Nag, A. Synthesis and Near-Infrared Emission of Yb-Doped $Cs_2AgInCl_6$ Double Perovskite Microcrystals and Nanocrystals. *J. Phys. Chem. C* **2019**, *123* (25), 15787−15793.

(24) Wang, S.; Qi, J.; Kershaw, S. V.; Rogach, A. L. Co-Doping of Cerium and Bismuth into Lead-Free Double Perovskite $Cs_2AgInCl_6$ Nanocrystals Results in Improved Photoluminescence Efficiency. *ACS Nanoscience Au* **2022**, *2* (2), 93−101.

(25) Locardi, F.; Cirignano, M.; Baranov, D.; Dang, Z.; Prato, M.; Drago, F.; Ferretti, M.; Pinchetti, V.; Fanciulli, M.; Brovelli, S.; et al. Colloidal Synthesis of Double Perovskite $Cs_2AgInCl_6$ and Mn-Doped $Cs_2AgInCl_6$ Nanocrystals. *J. Am. Chem. Soc.* **2018**, *140* (40), 12989−12995.

(26) Chen, N.; Cai, T.; Li, W.; Hills-Kimball, K.; Yang, H.; Que, M.; Nagaoka, Y.; Liu, Z.; Yang, D.; Dong, A.; et al. Yb- and Mn-Doped Lead-Free Double Perovskite Cs_2AgBiX_6 (X = Cl−, Br−) Nanocrystals. *ACS Appl. Mater. Interfaces* **2019**, *11* (18), 16855−16863.

(27) Das Adhikari, S.; Guria, A. K.; Pradhan, N. Insights of Doping and the Photoluminescence Properties of Mn-Doped Perovskite Nanocrystals. *J. Phys. Chem. Lett.* **2019**, *10* (9), 2250−2257.

(28) Han, P.; Zhang, X.; Luo, C.; Zhou, W.; Yang, S.; Zhao, J.; Deng, W.; Han, K. Manganese-Doped, Lead-Free Double Perovskite Nanocrystals for Bright Orange-Red Emission. *ACS Central Science* **2020**, *6* (4), 566−572.

(29) Su, X.; Lian, L.; Zhang, C.; Zhang, J.; Liu, S.; Zhu, S.; Gao, Y.; Luo, W.; Li, H.; Zhang, D. Enhanced Photoluminescence of Colloidal Lead-Free Double Perovskite $Cs_2Ag_{1-x}Na_xInCl_6$ Nanocrystals Doped with Manganese. *Advanced Optical Materials* **2021**, *9* (15), No. 2001866.

(30) Yang, H.; Shi, W.; Cai, T.; Hills-Kimball, K.; Liu, Z.; Dube, L.; Chen, O. Synthesis of lead-free $Cs_4(Cd_{1-x}Mn_x)Bi_2Cl_{12}$ ($0 \leq x \leq 1$) layered double perovskite nanocrystals with controlled Mn−Mn coupling interaction. *Nanoscale* **2020**, *12* (45), 23191−23199.

(31) Cai, T.; Wang, J.; Li, W.; Hills-Kimball, K.; Yang, H.; Nagaoka, Y.; Yuan, Y.; Zia, R.; Chen, O. Mn^{2+}/Yb^{3+} Codoped $CsPbCl_3$ Perovskite Nanocrystals with Triple-Wavelength Emission for Luminescent Solar Concentrators. *Advanced Science* **2020**, *7* (18), No. 2001317.

(32) Hills-Kimball, K.; Pérez, M. J.; Nagaoka, Y.; Cai, T.; Yang, H.; Davis, A. H.; Zheng, W.; Chen, O. Ligand Engineering for Mn^{2+} Doping Control in $CsPbCl_3$ Perovskite Nanocrystals via a Quasi-Solid−Solid Cation Exchange Reaction. *Chem. Mater.* **2020**, *32* (6), 2489−2500.

(33) Davis, A. H.; Hofman, E.; Chen, K.; Li, Z.-J.; Khammang, A.; Zamani, H.; Franck, J. M.; Maye, M. M.; Meulenberg, R. W.; Zheng, W. Exciton Energy Shifts and Tunable Dopant Emission in Manganese-Doped Two-Dimensional CdS/ZnS Core/Shell Nanoplatelets. *Chem. Mater.* **2019**, *31* (7), 2516−2523.

(34) Yang, H.; Cai, T.; Dube, L.; Hills-Kimball, K.; Chen, O. Synthesis of Ultrathin Perovskite Nanowires via a Postsynthetic Transformation Reaction of Zero-Dimensional Perovskite Nanocrystals. *Cryst. Growth Des.* **2021**, *21* (4), 1924−1930.

(35) Yang, H.; Cai, T.; Dube, L.; Chen, O. Synthesis of double perovskite and quadruple perovskite nanocrystals through post-synthetic transformation reactions. *Chemical Science* **2022**, *13* (17), 4874−4883.

(36) Yang, H.; Cai, T.; Liu, E.; Hills-Kimball, K.; Gao, J.; Chen, O. Synthesis and transformation of zero-dimensional Cs_3BiX_6 (X = Cl, Br) perovskite-analogue nanocrystals. *Nano Research* **2020**, *13* (1), 282−291.

(37) Hills-Kimball, K.; Nagaoka, Y.; Cao, C.; Chaykovsky, E.; Chen, O. Synthesis of formamidinium lead halide perovskite nanocrystals through solid−liquid−solid cation exchange. *Journal of Materials Chemistry C* **2017**, *5* (23), 5680−5684.

(38) Bateni, F.; Epps, R. W.; Abdel-latif, K.; Dargis, R.; Han, S.; Volk, A. A.; Ramezani, M.; Cai, T.; Chen, O.; Abolhasani, M. Ultrafast cation doping of perovskite quantum dots in flow. *Matter* **2021**, *4* (7), 2429−2447.

(39) Davis, A. H.; Li, S.; Lin, H.; Chu, C.; Franck, J. M.; Leem, G.; Maye, M. M.; Zheng, W. Ligand-mediated synthesis of chemically tailored two-dimensional all-inorganic perovskite nanoplatelets under ambient conditions. *Journal of Materials Chemistry C* **2021**, *9* (40), 14226−14235.

(40) Hills-Kimball, K.; Yang, H.; Cai, T.; Wang, J.; Chen, O. Recent Advances in Ligand Design and Engineering in Lead Halide Perovskite Nanocrystals. *Advanced Science* **2021**, *8* (12), No. 2100214.

(41) Ke, B.; Zeng, R.; Zhao, Z.; Wei, Q.; Xue, X.; Bai, K.; Cai, C.; Zhou, W.; Xia, Z.; Zou, B. Homo- and Heterovalent Doping-Mediated Self-Trapped Exciton Emission and Energy Transfer in Mn-Doped $Cs_2Na_{1-x}Ag_xBiCl_6$ Double Perovskites. *J. Phys. Chem. Lett.* **2020**, *11* (1), 340−348.

(42) Levy, S.; Khalfin, S.; Pavlopoulos, N. G.; Kauffmann, Y.; Atiya, G.; Shaek, S.; Dror, S.; Shechter, R.; Bekenstein, Y. The Role Silver Nanoparticles Plays in Silver-Based Double-Perovskite Nanocrystals. *Chem. Mater.* **2021**, *33* (7), 2370−2377.

(43) Wang, M.; Lyu, J.; Qin, X.; Yang, S.-W.; Liu, X.; Xu, G. Q. Direct Electron Transfer Enables Highly Efficient Dual Emission Modes of Mn^{2+}-Doped $Cs_2Na_{1-x}Ag_xBiCl_6$ Double Perovskites. *J. Phys. Chem. Lett.* **2022**, *13* (40), 9429−9434.

(44) Volonakis, G.; Haghighirad, A. A.; Milot, R. L.; Sio, W. H.; Filip, M. R.; Wenger, B.; Johnston, M. B.; Herz, L. M.; Snaith, H. J.; Giustino, F. $Cs_2InAgCl_6$: A New Lead-Free Halide Double Perovskite with Direct Band Gap. *J. Phys. Chem. Lett.* **2017**, *8* (4), 772−778.

(45) Vargas, B.; Reyes-Castillo, D. T.; Coutino-Gonzalez, E.; Sánchez-Aké, C.; Ramos, C.; Falcony, C.; Solis-Ibarra, D. Enhanced Luminescence and Mechanistic Studies on Layered Double-Perovskite Phosphors: $Cs_4Cd_{1-x}Mn_xBi_2Cl_{12}$. *Chem. Mater.* **2020**, *32* (21), 9307−9315.

(46) Wang, Z.; Zheng, W.; van Tol, J.; Dalal, N. S.; Strouse, G. F. High-field electron paramagnetic resonance as a microscopic probe of anisotropic strain at Mn^{2+} sites in $CdSe:Mn^{2+}$ quantum dots. *Chem. Phys. Lett.* **2012**, *524*, 73−77.

(47) Gan, W.; Cao, L.; Gu, S.; Lian, H.; Xia, Z.; Wang, J. Broad-Band Sensitization in Cr^{3+}−Er^{3+} Co-Doped $Cs_2AgInCl_6$ Double Perovskites with 1.5 μm Near-Infrared Emission. *Chem. Mater.* **2023**, *35* (14), 5291−5299.

(48) Pari, S.; Nandigana, P.; Panda, S. K. Tunable Warm to Cool White Light Emission from La-Doped and Na-Alloyed $Cs_2AgInCl_6$ Double Perovskites for Efficient Light-Emitting Diode Applications. *ACS Applied Optical Materials* **2023**, *1* (3), 802−809.

(49) Li, S.; Shi, Z.; Zhang, F.; Wang, L.; Ma, Z.; Wu, D.; Yang, D.; Chen, X.; Tian, Y.; Zhang, Y.; et al. Ultrastable Lead-Free Double Perovskite Warm-White Light-Emitting Devices with a Lifetime above 1000 h. *ACS Appl. Mater. Interfaces* **2020**, *12* (41), 46330−46339.

(50) Zheng, W.; Sun, R.; Liu, Y.; Wang, X.; Liu, N.; Ji, Y.; Wang, L.; Liu, H.; Zhang, Y. Excitation Management of Lead-Free Perovskite Nanocrystals Through Doping. *ACS Appl. Mater. Interfaces* **2021**, *13* (5), 6404−6410.

(51) Llanos, S.; Giraldo, L. J.; Santamaria, O.; Franco, C. A.; Cortés, F. B. Effect of Sodium Oleate Surfactant Concentration Grafted onto SiO2 Nanoparticles in Polymer Flooding Processes. *ACS Omega* **2018**, *3* (12), 18673−18684.

(52) Ma, Z.; Li, Q.; Luo, J.; Li, S.; Sui, L.; Zhao, D.; Yuan, K.; Xiao, G.; Tang, J.; Quan, Z.; et al. Correction to "Pressure-Driven Reverse Intersystem Crossing: New Path toward Bright Deep-Blue Emission of Lead-Free Halide Double Perovskites. *J. Am. Chem. Soc.* **2021**, *143* (45), 19240−19240.

(53) Luo, J.; Wang, X.; Li, S.; Liu, J.; Guo, Y.; Niu, G.; Yao, L.; Fu, Y.; Gao, L.; Dong, Q.; et al. Efficient and stable emission of warm-white light from lead-free halide double perovskites. *Nature* **2018**, *563* (7732), 541−545.

(54) Locardi, F.; Sartori, E.; Buha, J.; Zito, J.; Prato, M.; Pinchetti, V.; Zaffalon, M. L.; Ferretti, M.; Brovelli, S.; Infante, I.; De Trizio, L.; et al. Emissive Bi-Doped Double Perovskite $Cs_2Ag_{1-x}Na_xInCl_6$ Nanocrystals. *ACS Energy Letters* **2019**, *4* (8), 1976−1982.

(55) Zhang, Y.; Shah, T.; Deepak, F. L.; Korgel, B. A. Surface Science and Colloidal Stability of Double-Perovskite $Cs_2AgBiBr_6$ Nanocrystals and Their Superlattices. *Chem. Mater.* **2019**, *31* (19), 7962−7969.

(56) De Trizio, L.; Infante, I.; Manna, L. Surface Chemistry of Lead Halide Perovskite Colloidal Nanocrystals. *Acc. Chem. Res.* **2023**, *56* (13), 1815−1825.

(57) Smart, T. J.; Takenaka, H.; Pham, T. A.; Tan, L. Z.; Zhang, J. Z.; Ogitsu, T.; Ping, Y. Enhancing Defect Tolerance with Ligands at the Surface of Lead Halide Perovskites. *J. Phys. Chem. Lett.* **2021**, *12* (27), 6299−6304.

(58) Quarta, D.; Imran, M.; Capodilupo, A.-L.; Petralanda, U.; van Beek, B.; De Angelis, F.; Manna, L.; Infante, I.; De Trizio, L.; Giansante, C. Stable Ligand Coordination at the Surface of Colloidal $CsPbBr_3$ Nanocrystals. *J. Phys. Chem. Lett.* **2019**, *10* (13), 3715−3726.

(59) Chen, Z.; Chen, H.; Hu, H.; Yu, M.; Li, F.; Zhang, Q.; Zhou, Z.; Yi, T.; Huang, C. Versatile Synthesis Strategy for Carboxylic Acid−functionalized Upconverting Nanophosphors as Biological Labels. *J. Am. Chem. Soc.* **2008**, *130* (10), 3023−3029.

(60) Wheeler, L. M.; Sanehira, E. M.; Marshall, A. R.; Schulz, P.; Suri, M.; Anderson, N. C.; Christians, J. A.; Nordlund, D.; Sokaras, D.; Kroll, T.; Harvey, S. P.; et al. Targeted Ligand-Exchange Chemistry on Cesium Lead Halide Perovskite Quantum Dots for High-Efficiency Photovoltaics. *J. Am. Chem. Soc.* **2018**, *140* (33), 10504−10513.

(61) Zhang, B.; Wang, M.; Ghini, M.; Melcherts, A. E. M.; Zito, J.; Goldoni, L.; Infante, I.; Guizzardi, M.; Scotognella, F.; Kriegel, I.; et al. Correction to "Colloidal Bi-Doped $Cs_2Ag_{1-x}Na_xInCl_6$ Nanocrystals: Undercoordinated Surface Cl Ions Limit Their Light Emission Efficiency. *ACS Materials Letters* **2022**, *4* (9), 1756−1763.

(62) Fritzinger, B.; Capek, R. K.; Lambert, K.; Martins, J. C.; Hens, Z. Utilizing Self-Exchange To Address the Binding of Carboxylic Acid Ligands to CdSe Quantum Dots. *J. Am. Chem. Soc.* **2010**, *132* (29), 10195−10201.

(63) Gomes, R.; Hassinen, A.; Szczygiel, A.; Zhao, Q.; Vantomme, A.; Martins, J. C.; Hens, Z. Binding of Phosphonic Acids to CdSe Quantum Dots: A Solution NMR Study. *J. Phys. Chem. Lett.* **2011**, *2* (3), 145−152.

(64) De Roo, J.; Ibáñez, M.; Geiregat, P.; Nedelcu, G.; Walravens, W.; Maes, J.; Martins, J. C.; Van Driessche, I.; Kovalenko, M. V.; Hens, Z. Highly Dynamic Ligand Binding and Light Absorption Coefficient of Cesium Lead Bromide Perovskite Nanocrystals. *ACS Nano* **2016**, *10* (2), 2071−2081.

(65) Almeida, G.; Ashton, O. J.; Goldoni, L.; Maggioni, D.; Petralanda, U.; Mishra, N.; Akkerman, Q. A.; Infante, I.; Snaith, H. J.; Manna, L. The Phosphine Oxide Route toward Lead Halide Perovskite Nanocrystals. *J. Am. Chem. Soc.* **2018**, *140* (44), 14878−14886.

(66) Zeng, B.; Palui, G.; Zhang, C.; Zhan, N.; Wang, W.; Ji, X.; Chen, B.; Mattoussi, H. Characterization of the Ligand Capping of Hydrophobic CdSe−ZnS Quantum Dots Using NMR Spectroscopy. *Chem. Mater.* **2018**, *30* (1), 225−238.

(67) Ripka, E. G.; Deschene, C. R.; Franck, J. M.; Bae, I.-T.; Maye, M. M. Understanding the Surface Properties of Halide Exchanged Cesium Lead Halide Nanoparticles. *Langmuir* **2018**, *34* (37), 11139−11146.

(68) Hens, Z.; Martins, J. C. A Solution NMR Toolbox for Characterizing the Surface Chemistry of Colloidal Nanocrystals. *Chem. Mater.* **2013**, *25* (8), 1211−1221.

(69) Romero Esquivel, G.; Toader, V.; Reven, L.; Kambhampati, P. Ligand-flexible synthesis of strongly confined perovskite nanocrystals: a microwave synthetic approach. *Nanoscale* **2022**, *14* (42), 15789−15798.

(70) Ahmad, R.; Zdražil, L.; Kalytchuk, S.; Naldoni, A.; Rogach, A. L.; Schmuki, P.; Zboril, R.; Kment, Š. Uncovering the Role of Trioctylphosphine on Colloidal and Emission Stability of Sb-Alloyed $Cs_2NaInCl_6$ Double Perovskite Nanocrystals. *ACS Appl. Mater. Interfaces* **2021**, *13* (40), 47845−47859.

(71) Wang, B.-H.; Gao, B.; Zhang, J.-R.; Chen, L.; Junkang, G.; Shen, S.; Au, C.-T.; Li, K.; Cai, M.-Q.; Yin, S.-F. Thickness-induced band-gap engineering in lead-free double perovskite $Cs_2AgBiBr_6$ for highly efficient photocatalysis. *Phys. Chem. Chem. Phys.* **2021**, *23* (21), 12439−12448.

(72) Zhou, J.; Xia, Z.; Molokeev, M. S.; Zhang, X.; Peng, D.; Liu, Q. Composition design, optical gap and stability investigations of lead-

free halide double perovskite $Cs_2AgInCl_6$. *Journal of Materials Chemistry A* **2017**, 5 (29), 15031−15037.

(73) Yang, Z.; Wei, M.; Voznyy, O.; Todorovic, P.; Liu, M.; Quintero-Bermudez, R.; Chen, P.; Fan, J. Z.; Proppe, A. H.; Quan, L. N.; et al. Anchored Ligands Facilitate Efficient B-Site Doping in Metal Halide Perovskites. *J. Am. Chem. Soc.* **2019**, 141 (20), 8296−8305.

(74) Xue, S.; Wu, Q.; Huo, Q.; Mi, J.; Guan, C.; Cong, W.-Y.; Zhang, Z.; Ren, J.; Lu, Y.-B. Studies on the photoelectronic properties of a manganese (Mn)-doped lead-free double perovskite. *Phys. Chem. Chem. Phys.* **2022**, 24 (41), 25648−25655.

(75) van der Stam, W.; Geuchies, J. J.; Altantzis, T.; van den Bos, K. H. W.; Meeldijk, J. D.; Van Aert, S.; Bals, S.; Vanmaekelbergh, D.; de Mello Donega, C. Highly Emissive Divalent-Ion-Doped Colloidal $CsPb_{1−x}M_xBr_3$ Perovskite Nanocrystals through Cation Exchange. *J. Am. Chem. Soc.* **2017**, 139 (11), 4087−4097.

(76) Imran, M.; Ijaz, P.; Goldoni, L.; Maggioni, D.; Petralanda, U.; Prato, M.; Almeida, G.; Infante, I.; Manna, L. Simultaneous Cationic and Anionic Ligand Exchange For Colloidally Stable CsPbBr3 Nanocrystals. *ACS Energy Letters* **2019**, 4 (4), 819−824.